

The *Kepler* Smear Campaign I: An Asteroseismic Catalogue of Bright Red Giants

Benjamin J. S. Pope,^{1,2,3}★ Guy R. Davies,^{4,5} Keith Hawkins,^{6,7} Timothy R. White,^{5,8} Daniel Huber,^{9,10,11} Ashley Chontos,⁹ Victor Silva Aguirre,⁵ Victoria Antoci,⁵ Suzanne Aigrain,³ Timothy R. Bedding,^{10,5} Jie Yu,^{10,5} Amalie Stokholm,⁵ Timothy van Reeth,^{5,10} David W. Latham,¹² Allyson Bieryla,¹² Gilbert A. Esquerdo,¹² Paula Jofré,¹³ and friends

¹Center for Cosmology and Particle Physics, Department of Physics, New York University, 726 Broadway, New York, NY 10003, USA

²NASA Sagan Fellow

³Oxford Astrophysics, Denys Wilkinson Building, University of Oxford, OX1 3RH, Oxford, UK

⁴School of Physics and Astronomy, University of Birmingham, Birmingham B15 2TT, UK

⁵Stellar Astrophysics Centre, Department of Physics and Astronomy, Aarhus University, Ny Munkegade 120, DK-8000 Aarhus C, Denmark

⁶Department of Astronomy, The University of Texas at Austin, 2515 Speedway Boulevard, Austin, TX 78712, USA

⁷Department of Astronomy, Columbia University, 550 W 120th St, New York, NY 10027, USA

⁸Research School of Astronomy and Astrophysics, Mount Stromlo Observatory, The Australian National University, Canberra, ACT 2611, Australia

⁹Institute for Astronomy, University of Hawai'i, 2680 Woodlawn Drive, Honolulu, HI 96822, USA

¹⁰Sydney Institute for Astronomy (SIfA), School of Physics, University of Sydney, NSW 2006, Australia

¹¹SETI Institute, 189 Bernardo Avenue, Mountain View, CA 94043, USA

¹²Harvard-Smithsonian Center for Astrophysics, 60 Garden Street, Cambridge, MA 02138, USA

¹³Núcleo de Astronomía, Facultad de Ingeniería y Ciencias, Universidad Diego Portales, Ejército 441, Santiago De, Chile

Accepted XXX. Received YYY; in original form ZZZ

ABSTRACT

Here we present the first data release of the *Kepler* Smear Campaign, using collateral ‘smear’ data obtained by *Kepler* to reconstruct light curves of 102 stars too bright to have been otherwise targeted. We describe the pipeline developed to extract and calibrate these light curves, and show that we attain photometric precision comparable to stars analyzed by the standard pipeline in the nominal *Kepler* mission. In this Paper, we focus in particular on a subset of these consisting of 64 red giants for which we detect solar-like oscillations. Using high-resolution spectroscopy from the Tillinghast Reflector Échelle Spectrograph (TRES) together with asteroseismic modelling, we obtain the stellar densities and derive masses, radii and ages of 34 of these red giant and red clump stars as benchmarks. All source code, light curves, TRES spectra, and asteroseismic and stellar parameters are publicly available as a *Kepler* legacy sample.

Key words: asteroseismology – techniques: photometric – stars: variable: general

1 INTRODUCTION

Kepler has revolutionized the field of asteroseismology for solar-like oscillations (Gilliland et al. 2010; Chaplin et al. 2010). It has yielded the detection of gravity-mode period spacings in a red giant (Beck et al. 2011; Mosser et al. 2014), enabling probes of interior rotation of red giants (Beck et al. 2012; Mosser et al. 2012b) and distinguishing between hydrogen- and helium-burning cores (Bedding et al. 2011; Mosser et al. 2012a). It has also permitted the determination of ages and fundamental parameters of main-sequence stars

as cool as the Sun and hotter (Silva Aguirre et al. 2013), including planet-hosting stars (Huber et al. 2013; Silva Aguirre et al. 2015; Van Eylen et al. 2018), revealing the most ancient known planetary system, dating back to the earliest stages of the galaxy (Campante et al. 2015). By comparing asteroseismic stellar ages to stellar rotation periods, Angus et al. (2015) have shown that gyrochronology models cannot fit the data with a single relation, leading van Saders et al. (2016) to suggest a qualitative change in dynamo mechanism as stars age through the main sequence.

★ E-mail: benjamin.pope@nyu.edu

A major outcome of the *Kepler* asteroseismology programme is a legacy sample of extremely well characterized stars that can serve as benchmarks for future work (Lund et al. 2016; Silva Aguirre et al. 2016). Asteroseismological studies with *Kepler* complement other probes of stellar physics well: for example, the APOKASC sample of 1916 spectroscopically- and asteroseismically-characterized red giant stars (Pinsonneault et al. 2014). For this APOKASC sample, Hawkins et al. (2016c) have been able to extract precise elemental abundances by fitting spectroscopic data with $\log g$ and T_{eff} fixed to asteroseismically-determined values. It is necessary to calibrate such a study against benchmark stars with very precisely-determined parameters, which in practice requires nearby bright stars that are amenable to very high signal-to-noise spectroscopy plus asteroseismology (Creevey et al. 2013), parallaxes (Hawkins et al. 2016a), and/or interferometry (Casagrande et al. 2014; Creevey et al. 2015). This is especially important in the context of the *Gaia* mission (Gaia Collaboration et al. 2016), which has recently put out its second data release of 1,692,919,135 sources, including 1,331,909,727 with parallaxes (Gaia Collaboration et al. 2018). These data will form the basis of many large surveys and it is vital that they are calibrated correctly. To this end, 34 FGK stars including both giants and dwarfs have been chosen as *Gaia*-ESO benchmark stars for which metallicities (Jofré et al. 2014), effective temperatures and asteroseismic surface gravities (Heiter et al. 2015), and relative abundances of α and iron-peak elements (Jofré et al. 2015) have been determined. This includes only four main sequence stars much cooler than the Sun, due to the paucity of such stars with asteroseismology. This has been accompanied by the release of high resolution spectra (Blanco-Cuaresma et al. 2014) and formed the basis of extensions to lower metallicities (Hawkins et al. 2016b), stellar twin studies (Jofré 2016) and comparisons of stellar abundance determination pipelines (Jofré et al. 2017). Furthermore, by combining asteroseismology with optical interferometry, it has been possible to determine fundamental parameters of main-sequence and giant stars with unprecedented precision (Huber et al. 2012; White et al. 2013, 2015).

Brighter *Kepler* stars are therefore ideal benchmark targets, since photometry can be most easily complemented by *Gaia* parallaxes, interferometric diameters, and high resolution spectroscopy. Unfortunately, the *Kepler* field was deliberately placed to minimize overall the number of extremely bright stars on the detectors, so that only a dozen stars brighter than 6th magnitude landed on silicon (Koch et al. 2010). This was because stars brighter than $Kp \sim 11$ saturate the CCD detectors, with their flux distributed along a bleed column and rendering those pixels otherwise unusable. Furthermore, due to the limited availability of bandwidth to download data from the spacecraft, only a fraction **What fraction?** of pixels on the *Kepler* detectors are actually downloaded. The result of these two target selection constraints is that photometry was obtained for only **a small number** of saturated stars in the *Kepler* field, while many bright targets were ignored. In the *K2* mission (Howell et al. 2014), very saturated stars have been observed with ‘halo photometry’ using unsaturated pixels in a specially-determined region around bright stars, including the Pleiades (White et al. 2017), Aldebaran (Farr et al. 2018), and ρ Leonis (Aerts et al. 2018). Unfortunately, in the legacy *Kepler* sample, photometry of such saturated stars was rarely attempted.

Kołodziejczak & Caldwell (2011) noted a way to obtain photometry of every target on-silicon in *Kepler* using a data channel normally used for calibration, even if active pixels were not allocated and downloaded. *Kepler* employs an inter-line transfer CCD as its detector, which successively shuffles each row of pixels down

to the edges of the chip to be read out. Because the *Kepler* camera lacks a shutter, the detector is exposed to light during the readout process, with the result that fluxes in each pixel are contaminated by light collected from objects in the same column. This is a particularly serious issue for faint objects in the same detector column as brighter stars, and it is important to calibrate this at each readout stage. Six rows of blank ‘masked’ pixels were allocated in each column to measure the smear bias; furthermore, six ‘virtual’ rows were recorded at the end of the readout, with the result that twelve rows of pixels sample the smear bias in each column. Kołodziejczak & Caldwell (2011) realized that these encode the light curves of bright targets in a 1D projection of the star field. The masked and virtual smear registers each receive $\sim 1/1034$ of the incident flux in each column. If this is dominated by the light from a single star, the flux combining both smear registers is equivalent to that of a star ~ 6.8 times fainter.

In Pope et al. (2016), we demonstrated a method for extracting precise light curves of bright stars in *Kepler* and *K2*, and presented light curves of a small number of variable stars as examples to illustrate this method. In this paper we present smear light curves of all unobserved or significantly under-observed stars brighter than $Kp = 9$ in the *Kepler* field. This sample mostly consists of red giants and hot stars, containing only a few FG dwarfs. We find no transiting planets, but detect **M** new eclipsing binaries, and measure solar-like oscillations in 34 red giants. We do not model hot stars or FG dwarfs in great detail, but provide some discussion and initial classification of interesting variability. For eclipsing binaries, we present the results of light-curve modelling to precisely determine their parameters. For the oscillating red giants that constitute the bulk of the sample, we determine the asteroseismic parameters ν_{max} and $\Delta\nu$, and therefore stellar masses and $\log g$ measurements. We have also obtained high-resolution optical spectroscopy of 63 objects, predominantly giants, with the Tillinghast Reflector Échelle Spectrograph (TRES). For the 34 stars with both spectroscopy and asteroseismic parameters we derive fundamental stellar parameters and elemental abundances. These asteroseismic constraints can be compared to those from *Gaia*, offering the opportunity both to test asteroseismic scaling relations and combine both datasets to refine the benchmark star properties further.

We have made all new data products and software discussed in this paper publicly available, and encourage interested readers to use these in their own research.

2 METHOD

We have obtained smear light curves for our sample of red giant stars with the `keplersmear` pipeline as described in Section 2.2, performed asteroseismology on all of these to extract ν_{max} and therefore $\log g$ as described in Section 2.3, and combined these with TRES spectra to obtain chemical abundances as described in Section 2.4.

2.1 Sample

We selected as our sample all stars on-silicon in *Kepler* with $Kp < 9$ that were targeted for fewer than an arbitrary 8 quarters, the majority of which were previously entirely missing. Sixteen stars were to some extent observed conventionally: HD 174020 was targeted in LC for Q2, 6, 10, and 14; HD 175841 for Q11-12, 14-16, with SC for Q3; HD 176582 for Q12-13; HD 178090 for Q1, 3, and 10; HD 180682 for Q0, 3, and 7; HD 181069 for Q1, 10, 13, 14, and 17;

HD 181878 for Q14-17; HD 182694 for Q2; HD 183124 for even quarters; HD 185351 for Q1-3 and with SC for Q16; HD 186155 for only Q1; HD 187217 for Q14-17; HD 188252 for only Q13; HD 189013 with SC for Q3 as a γ Dor; V380 Cyg for Q11 and with SC for Q7, 9, 10, 12-17; and V819 Cyg for Q14, 16 and 17. A number of these lay at the edge of a detector, with the result that in some cadences the centroid of the star did not lie on the chip; light curves from these targets were found to be of extremely low quality and all of these objects were discarded. After applying these criteria we obtained a list of 102 targets, which are listed in Table 1 with their *Kepler* magnitude K_p together with their spectral type from SIMBAD, *Gaia* DR2 apparent G magnitudes and $B_p - R_p$ colours, *Gaia* DR2 calibrated distances from Bailer-Jones et al. (2018), variability classification and availability of TRES spectroscopy. A Venn diagram of the sample, noting the availability of asteroseismic fits Section 2.3 and spectroscopy (Section 2.4) is displayed in Figure 2. The *Kepler* spacecraft rotates between quarters, so that it cycles through four orientation ‘seasons’ each rotated from the last by 90° . Some stars did not land on silicon for all seasons: we have only one season of HD 179394; two for HD 187277, HD 226754, V554 Lyr, and BD+47 2891; and three for BD+43 3064. **Aside from the restriction on stars falling on the edge of a chip**, the addition of our sample to the conventionally-observed stars makes the *Kepler* survey magnitude-complete down to $K_p = 9$.

Figure 1 shows these stars on a colour-magnitude diagram in *Gaia* $B_p - R_p$ and absolute G magnitudes using *Gaia* DR2 calibrated distances from Bailer-Jones et al. (2018), overlaid on the *Kepler* sample from the Bedell gaia-kepler.fun crossmatch. The smear targets in this diagram appear to have not merely higher apparent brightnesses than the general *Kepler* population, but also higher intrinsic luminosities. While this could simply arise from being selected for their apparent brightness, it is worth considering whether this is because of a bias in their parallax measurements. While *Gaia* parallaxes for very bright stars can be subject to systematic error, we have compared these to those found by *Hipparcos* (van Leeuwen 2007), and found close agreement for the brightest stars, with a scatter that increases with magnitude. We therefore suggest that parallax bias is not the reason for the smear sample sitting above the remainder of the *Kepler* sample.

We identify the evolutionary state of objects in the main sequence versus evolved stars first from the *Gaia* colour-magnitude diagram in Figure 1. Taking a cutoff in *Gaia* $B_p - R_p > 1$, we identify 64 of these objects as clearly evolved systems, and the remaining 38 lie apparently on the main sequence.

One of the main sequence objects, BD+43 3068 is a G0 dwarf with a G magnitude of 8.267944 and a distance of 53.8 ± 0.1 pc, and it is therefore surprising that it was not included in the nominal *Kepler* survey as a Solar analogue: it is possible that it was previously misidentified as a giant. Regrettably, it is only possible to reconstruct a light curve with the 30 minute long cadence and therefore it is not possible to do asteroseismology on this bright, nearby solar-like star. This light curve shows neither rotational modulation (as determined by its featureless autocorrelation) nor evidence for transits.

Considering objects lying photometrically on the main sequence, from the *Kepler* power spectrum we identify solar-like oscillations in HD 182354 and HD 176209 at frequencies consistent with them being subgiants or contaminated with flux from red giants. **Get frequencies.**

2.2 Photometry

In preparing light curves of the *Kepler* smear stars, we have followed the methods described in Pope et al. (2016), with some improvements. We selected our input RA and Dec values from the *Kepler* Input Catalog (KIC) (Brown et al. 2011), and queried MAST to find the corresponding mean pixel position for a given *Kepler* quarter. We then measured the centroid of smear columns in the vicinity, and used these values to do raw aperture photometry. We found that the cosine-bell aperture used for raw photometry in Pope et al. (2016) can in some light curves introduce position-dependent systematics and jumps. We instead in this work have applied a super-Gaussian aperture, $A \propto \exp \frac{-(x - x_0)^4}{w}$, where x_0 is the centroid and w a width in pixels. The very flat top of this function helps avoid significant variation with position, while still smoothly rolling off at the edges to avoid discontinuous artefacts. This is calculated on a grid of $10 \times$ subsampled points in pixel space so that the sharply varying edge changes column weights smoothly as a function of centroid. We have then extracted photometry using apertures with a range of widths $w \in \{1.5, 2, 3, 4, 5\}$ pixels.

From this raw photometry a background light curve was subtracted, which corrects for time-varying global systematics. Whereas in Pope et al. (2016) we subtracted a background estimate chosen manually, for this larger set of light curves, we have now chosen the lowest 25% of pixels by median flux as being unlikely to be contaminated by stars, and taken our background level to be the median of this at each time sample. To denoise this, we fit a Gaussian Process with a 30-day timescale squared exponential kernel using GEORGE (Ambikasaran et al. 2015), and our final background light curve is taken to be the posterior mean of this GP.

The dominant source of residual systematic errors in nominal *Kepler* time series is a common-mode variation primarily due to thermal changes on board the spacecraft, an issue which is traditionally dealt with by identifying and fitting a linear combination of systematic modes (Twicken et al. 2010; Stumpe et al. 2012; Smith et al. 2012; Petigura & Marcy 2012). We have adopted the same approach here, using the *Kepler* Pre-search Data Conditioning (PDC) Cotrending Basis Vectors (CBVs) available from MAST, finding least-squares fits of either the first 4 or 8 CBVs to each light curve. This can subtract astrophysical signals on long timescales, such that we use and recommend 4 CBV light curves for stars with variability on timescales longer than ~ 5 days, or indeed raw uncorrected lightcurves for stars variable at high amplitude on \sim quarter timescales, but otherwise we recommend the 8 CBV light curves. There is some room for improvement here by simultaneously modelling astrophysical and instrumental variations, but this is beyond the scope of this paper. In the following, we will use the light curves with the lowest 6.5 hr Combined Differential Photometric Precision (CDPP) (Christiansen et al. 2012) out of all apertures, as calculated with the $\kappa 2sc$ implementation (Aigrain et al. 2016). This is not necessarily the optimal choice for all red giants, especially those with oscillations on a 6.5 h timescale, but is a reasonable proxy nevertheless for white noise and leads to satisfactory results upon visual inspection of the present sample.

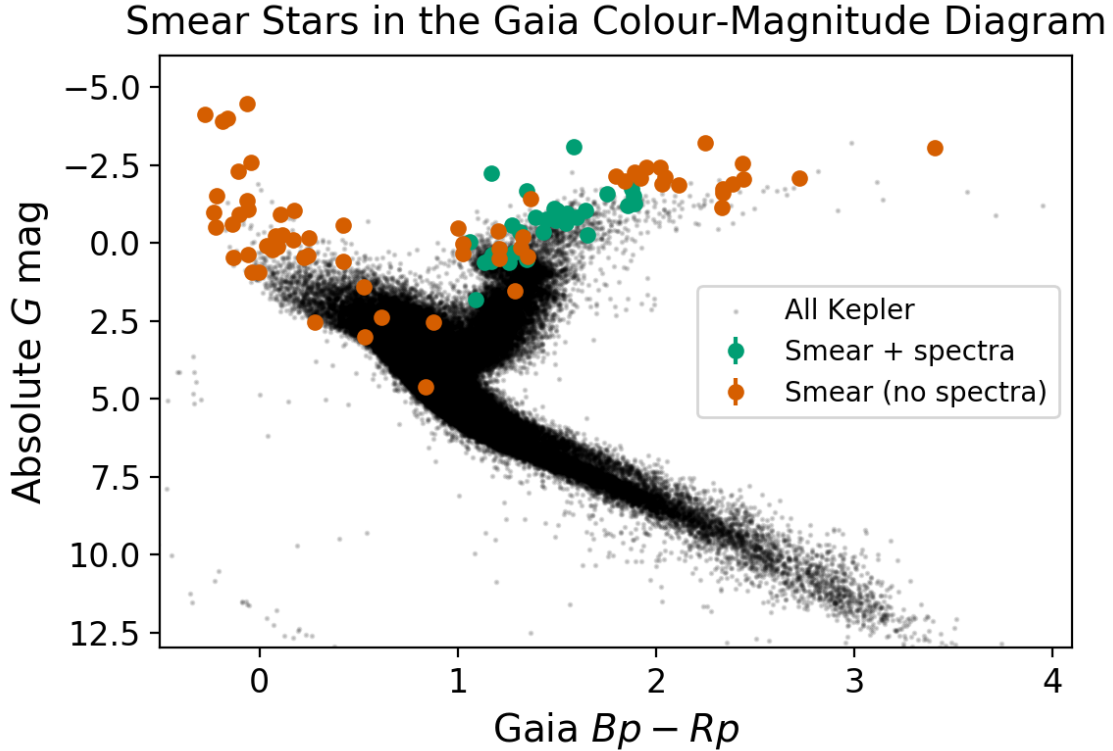


Figure 1. *Gaia* colour-magnitude diagram of the Smear Campaign stars (orange and teal) overlaid on the sample of *Kepler* stars with *Gaia* parallax SNR > 25 (black), using the Bedell [gaia-kepler.fun](https://github.com/bedell/gaia-kepler.fun) crossmatch and *Gaia* DR2 calibrated distances from [Bailer-Jones et al. \(2018\)](https://arxiv.org/abs/201801084). The smear sample includes giants and hot main-sequence stars. Those giants for which TRES spectroscopy have been obtained are highlighted in teal. An interactive version of this diagram is available as supplementary material from the journal or at benjaminpope.github.io/data/cmd_smear.html.

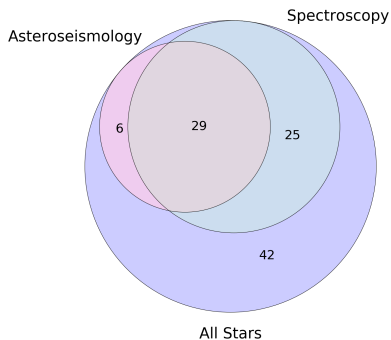


Figure 2. Venn diagram showing the overall structure of the *Kepler* Smear Campaign sample, showing the subsets for which TRES spectroscopy and asteroseismology are available and their overlap.

Because the smear data are collected along an entire CCD column, there is the risk of contamination from sufficiently bright sources. This is especially true in doing asteroseismology of red giants, where the low-amplitude stochastically-excited oscillations can be washed out in a power spectrum by the coherent high amplitude variations of a classical pulsator, even if the background star is much fainter. We can assess the importance of this contamination by considering the differences between odd and even quarters: because

the *Kepler* spacecraft rotates 90° between successive quarters, any contaminant will lie in the same column as a smear target only every second quarter, falling in the other quarters in the same row but not necessarily the same column. We have therefore generated Lomb-Scargle periodograms ([Lomb 1976](https://arxiv.org/abs/1976); [Scargle 1982](https://arxiv.org/abs/1982)) of each light curve, clipped for outliers, and considering only odd and even quarters, and visually inspected these for significant differences. In the great majority of cases they closely resemble one another, indicating that contamination is at worst a minor effect. In the case of HD 181878, a red giant, there is clear and significant contamination from an M giant, as is seen in Figure 3. Likewise HD 183383 shows two different stars, depending on the quarter: some parts are likely from an ellipsoidal variable with a period of 6.46 days, other parts are from an RR Lyrae pulsator.

2.3 Asteroseismology

While 64 red giants have been identified in this sample, for some of these, by visual inspection it is clear that the timescale of their variability is of the same order as a *Kepler* quarter and they are thus badly affected by systematics and systematics correction. In Table 1 we have noted these as ‘long-period variables’ (LPVs), without specifically meaning these are LPVs by a particular astrophysical definition, and they are discussed further in Section 3.1.3. For the 34 giants for which there is high-SNR shorter-timescale variability, we have attempted to extract the asteroseismic parameters ν_{\max} and $\langle \Delta \nu \rangle$ ([Kjeldsen & Bedding 1995](https://arxiv.org/abs/1995); [Chaplin & Miglio 2013](https://arxiv.org/abs/2013)). These

Table 1. The full set of underobserved and unobserved stars for which new light curves have been produced in this smear catalogue. Calibrated *Gaia* distances are from Bailer-Jones et al. (2018). Some objects, such as HD 185351, were observed in long cadence in some quarters and short cadence in others, and this is noted accordingly. The eclipsing binary V2083 Cyg was detected by *Gaia*, but a parallax could not be obtained in DR2, possibly due to binary motion. Variability classes are determined by inspection, having their usual abbreviations. EV denotes an ellipsoidal variable, but some of these could be rotation and spot modulation. γ Dor/ δ Sct denotes a γ Dor/ δ Sct hybrid, not uncertainty. H+S denotes a ‘hump and spike’ star. Question marks indicate uncertainty, and dashes – that no significant variability is observed.

Object	KIC	Spectral Type (SIMBAD)	<i>Kp</i> (mag)	<i>G</i> (mag)	<i>Bp</i> – <i>Rp</i> (mag)	<i>Gaia</i> Distance (pc)	TRES	Variability Class
14 Cyg	7292420	G8.5IIbFe-0.5	5.490	4.882	1.091	41.2 ^{+0.1} _{-0.1}	–	EV
BD+36 3564	1575741	F5II-III	8.128	4.923	0.529	50.6 ^{+0.4} _{-0.4}	✓	RG
BD+39 3577	4989821	G8III	8.131	5.152	1.171	81.5 ^{+0.6} _{-0.6}	✓	RG
BD+39 3882	4850372	A2V	8.259	5.279	0.107	172.6 ^{+3.3} _{-3.2}	–	Irregular
BD+42 3150	7091342	B9III	8.350	5.370	-0.055	194.3 ^{+7.0} _{-6.6}	–	?
BD+42 3367	7447756	B5V	7.271	5.410	-0.106	347.3 ^{+13.0} _{-12.1}	✓	LPV
BD+42 3393	6870455	M1III	7.664	5.313	2.047	306.4 ^{+10.3} _{-9.6}	✓	LPV
BD+43 3064	8075287	G7IIIa	8.284	5.598	1.061	133.1 ^{+0.7} _{-0.7}	✓	RG
BD+43 3068	8006792	B1.1III+B2.5/3V:	8.308	5.632	-0.062	1044.7 ^{+116.6} _{-95.6}	–	–
BD+43 3171	7810954	M3III	8.373	5.176	2.250	475.2 ^{+35.1} _{-30.7}	✓	LPV
BD+43 3213	7747499	A5III	8.311	5.881	0.246	125.2 ^{+30.7} _{-5.7}	✓	LPV
BD+47 2825	10337574	B2III	8.251	5.864	-0.276	1000.6 ^{+82.6} _{-71.1}	–	EB
BD+47 2891	10347606	K1III	8.680	5.985	1.283	135.8 ^{+0.3} _{-0.3}	–	RG
BD+48 2904	11085556	K5	8.487	6.055	1.645	263.5 ^{+3.8} _{-3.8}	–	RG
BD+48 2955	10988024	K2	7.961	6.091	1.584	683.8 ^{+12.4} _{-11.9}	✓	RG
HD 174020	7800227	K2	6.753	5.919	nan	397.8 ^{+6.8} _{-6.6}	✓	RG
HD 174177	9630812	M4-IIIa	6.575	5.228	2.725	288.9 ^{+13.1} _{-12.0}	–	γ Dor
HD 174676	7420037	K0	7.481	6.144	1.448	238.9 ^{+12.0} _{-11.4}	✓	LPV
HD 174829	7339102	K1III	6.967	6.264	1.237	144.2 ^{+0.6} _{-0.6}	✓	RG
HD 175132	6020867	K0	6.362	6.258	1.168	499.2 ^{+7.2} _{-7.0}	–	EV
HD 175466	7340766	B3V	6.165	6.160	-0.217	345.1 ^{+3.6} _{-3.6}	–	LPV
HD 175740	6265087	K0	5.212	6.291	nan	228.9 ^{+1.7} _{-1.7}	✓	RG
HD 175841	4989900	B9IIpSi	6.885	6.242	-0.063	333.3 ^{+5.9} _{-5.7}	–	γ Dor/ δ Sct
HD 175884	6584587	B0.5IIIn	6.210	6.243	-0.160	1114.0 ^{+70.9} _{-63.0}	✓	RG
HD 176209	9327530	B3Ve	7.437	6.208	-0.041	571.1 ^{+18.2} _{-17.2}	–	?
HD 176582	4136285	K0	6.510	6.345	1.273	243.2 ^{+1.8} _{-1.8}	–	EV
HD 176626	7943968	G8II	6.933	6.395	1.176	160.7 ^{+0.8} _{-0.8}	–	EV
HD 176894	6267965	M0II-III	7.700	6.171	2.031	409.4 ^{+3.8} _{-3.7}	–	γ Dor
HD 177697	4994443	K5	7.300	6.248	1.892	317.7 ^{+2.7} _{-2.7}	–	RG
HD 177781	2970780	B5V	7.744	6.383	-0.232	298.6 ^{+3.9} _{-3.8}	–	γ Dor/ δ Sct
HD 178090	6675338	A2IV	6.758	6.483	0.119	223.9 ^{+1.7} _{-1.6}	–	LPV
HD 178797	10064283	K0	7.312	6.532	1.486	295.8 ^{+2.5} _{-2.5}	✓	RG
HD 178910	11288450	G5	7.864	6.587	1.003	259.5 ^{+1.8} _{-1.8}	✓	RG
HD 179394	7105221	K5	7.575	6.600	1.754	433.1 ^{+4.2} _{-4.1}	✓	–
HD 179395	6593264	A0V	7.168	6.658	-0.003	139.6 ^{+1.1} _{-1.1}	–	EV
HD 179396	3838362	K5	8.001	6.549	1.892	583.0 ^{+8.5} _{-8.3}	✓	RG
HD 179959	10265370	K4III	6.280	6.696	1.798	585.0 ^{+9.1} _{-8.9}	✓	RG
HD 180312	4551179	A2	7.970	6.797	0.172	241.0 ^{+2.1} _{-2.1}	✓	RG
HD 180475	11656042	A3	7.664	6.810	0.351	–	✓	RG
HD 180658	6195870	A2	7.932	6.840	0.225	188.8 ^{+6.4} _{-6.0}	✓	RG
HD 180682	5177450	K5	6.617	6.530	2.116	476.9 ^{+5.9} _{-5.8}	✓	LPV
HD 181022	3946721	A2V	6.496	6.841	0.035	224.8 ^{+1.8} _{-1.7}	✓	LPV
HD 181069	4049174	A0	6.279	6.852	0.059	217.8 ^{+3.4} _{-3.3}	✓	RG
HD 181097	4149233	A5	7.920	6.855	0.421	180.0 ^{+1.0} _{-1.0}	✓	RG
HD 181328	12456737	A3	7.182	6.862	0.252	254.5 ^{+4.1} _{-4.0}	✓	LPV
HD 181521	5180075	K0	6.939	6.928	1.391	355.0 ^{+3.5} _{-3.4}	–	γ Dor/ δ Sct
HD 181596	11910615	M3	7.050	5.403	3.406	494.7 ^{+34.9} _{-30.6}	✓	RG
HD 181597	11555267	K5III	6.040	6.863	1.841	591.1 ^{+8.1} _{-7.8}	✓	RG
HD 181681	5092997	B9	6.864	7.070	0.067	233.9 ^{+1.7} _{-1.7}	✓	RG
HD 181778	7816792	B8V	7.545	7.034	-0.221	321.5 ^{+3.7} _{-3.6}	✓	RG
HD 181878	4830109	M1	6.698	6.614	2.334	353.9 ^{+3.3} _{-3.3}	✓	RG
HD 181880	3337423	M5	7.982	6.719	2.337	492.9 ^{+5.5} _{-5.4}	✓	RG

Table 1 – *continued* The full set of underobserved and unobserved stars for which new light curves have been produced in this smear catalogue. Calibrated *Gaia* distances are from [Bailer-Jones et al. \(2018\)](#).

Object	KIC	Spectral Type (SIMBAD)	<i>Kp</i> (mag)	<i>G</i> (mag)	<i>Bp</i> – <i>Rp</i> (mag)	<i>Gaia</i> Distance (pc)	TRES	Variability Class
HD 182354	2156801	B9	6.320	7.143	-0.055	226.5 ^{+2.4} _{-2.3}	–	RG
HD 182531	11188366	B9IV	7.955	7.145	-0.037	175.5 ^{+2.6} _{-2.5}	✓	RG
HD 182692	10728753	M0	7.310	6.992	2.020	762.0 ^{+15.8} _{-15.2}	✓	RG
HD 182694	7680115	K5	5.722	6.764	2.338	472.0 ^{+3.4} _{-3.3}	✓	RG
HD 182737	1572070	K0	7.820	7.247	1.227	226.6 ^{+1.3} _{-1.3}	–	LPV
HD 183124	8752618	K0	6.441	7.249	1.478	406.1 ^{+4.8} _{-4.7}	✓	RG
HD 183203	12208512	B8	6.928	7.189	-0.135	361.2 ^{+6.4} _{-6.1}	✓	LPV
HD 183362	2715115	K0	6.394	7.324	1.345	629.9 ^{+11.4} _{-11.0}	–	H+S
HD 183383	6777469	M3III	7.640	6.784	2.443	587.8 ^{+13.1} _{-12.6}	–	EV
HD 184147	9651435	A0	7.251	7.365	0.091	282.2 ^{+2.7} _{-2.7}	–	EV
HD 184215	11031549	–	7.321	7.440	2.434	993.3 ^{+26.7} _{-25.4}	–	γ Dor
HD 184483	7756961	M0	7.246	6.917	2.388	581.7 ^{+9.2} _{-8.9}	✓	LPV
HD 184565	6047321	K0	7.972	7.514	1.315	374.5 ^{+3.4} _{-3.4}	–	LPV
HD 184787	6528001	B8	6.757	7.475	-0.100	476.2 ^{+12.2} _{-11.6}	✓	H+S
HD 184788	6129225	A0	7.249	7.464	0.282	96.9 ^{+0.4} _{-0.4}	–	?
HD 184875	6954647	B0III	5.403	7.451	-0.185	1866.1 ^{+138.1} _{-120.6}	–	EV
HD 185117	9094435	B9	7.696	7.537	0.081	357.1 ^{+5.5} _{-5.3}	–	LPV
HD 185286	7966681	K2	6.151	7.595	1.489	546.1 ^{+8.0} _{-7.8}	✓	RG
HD 185351	8566020	K5	5.034	7.414	1.952	929.0 ^{+25.9} _{-24.5}	✓	RG
HD 185397	3455268	K5	6.953	7.472	1.921	817.7 ^{+14.8} _{-14.3}	–	δ Sct
HD 185524	8960196	F0	8.022	7.610	0.530	82.8 ^{+0.2} _{-0.2}	✓	LPV
HD 186121	7456762	K5	5.773	7.546	1.888	651.0 ^{+12.0} _{-11.6}	✓	LPV
HD 186155	9163520	G5	5.055	7.701	1.024	296.2 ^{+2.6} _{-2.5}	–	EV
HD 186255	4937492	A0	6.966	7.758	0.421	460.3 ^{+6.7} _{-6.5}	–	δ Sct
HD 186727	12316020	K2	7.499	7.702	1.652	391.8 ^{+6.1} _{-5.9}	✓	LPV
HD 186994	8766240	K2	7.585	7.848	1.346	291.3 ^{+5.4} _{-5.2}	–	EB
HD 187217	11824273	K0	6.399	7.848	1.434	434.3 ^{+6.2} _{-6.0}	✓	RG
HD 187277	6967644	K0	7.579	7.871	1.256	282.2 ^{+2.3} _{-2.3}	–	–
HD 187372	10679281	K5	5.672	7.859	1.502	599.3 ^{+9.2} _{-8.9}	✓	LPV
HD 188252	10683303	K2	6.007	7.899	1.549	589.4 ^{+11.6} _{-11.1}	–	γ Dor
HD 188537	9110718	K0II	7.382	7.834	1.162	290.5 ^{+2.4} _{-2.4}	✓	RG
HD 188629	8710324	K0	7.743	7.943	1.024	380.9 ^{+4.3} _{-4.2}	✓	LPV
HD 188875	5041881	K	6.164	7.940	1.498	541.2 ^{+10.1} _{-9.7}	✓	RG
HD 189013	10096499	K2	6.922	7.970	1.244	321.2 ^{+2.7} _{-2.6}	–	γ Dor
HD 189178	5219588	K2	5.552	7.953	1.368	753.4 ^{+15.9} _{-15.2}	–	γ Dor
HD 189636A	10298067	–	8.025	8.118	1.211	384.7 ^{+6.0} _{-5.8}	–	?
HD 189636B	10298061	K0	8.107	8.061	1.207	327.0 ^{+3.8} _{-3.8}	–	?
HD 189684	9305008	–	5.982	8.024	1.316	376.4 ^{+4.9} _{-4.7}	–	EV
HD 189750	8521828	K5	8.052	8.041	1.544	547.1 ^{+11.6} _{-11.1}	–	?
HD 190149	8262528	G5	6.488	8.090	1.134	311.7 ^{+2.7} _{-2.7}	✓	LPV
HD 226754	6234579	–	7.829	8.092	-0.129	335.7 ^{+4.6} _{-4.5}	✓	RG
V2079 Cyg	8818020	K0	7.174	8.236	1.329	485.8 ^{+7.3} _{-7.1}	–	EV
V2083 Cyg	10342012	F5	6.902	8.159	0.616	143.3 ^{+0.7} _{-0.7}	–	EB
V380 Cyg	5385723	K5	5.771	8.203	1.599	641.0 ^{+20.3} _{-19.1}	–	EB
V398 Lyr	4042516	G0	7.024	8.268	0.839	53.8 ^{+0.1} _{-0.1}	✓	RG
V543 Lyr	5429169	K5	6.299	8.139	1.876	948.8 ^{+25.8} _{-24.5}	–	SPB
V546 Lyr	6267345	K0	7.385	8.315	1.206	546.0 ^{+32.5} _{-29.1}	✓	LPV
V547 Lyr	5429948	M0	6.199	8.178	1.858	751.5 ^{+17.2} _{-16.5}	✓	LPV
V554 Lyr	5001462	K0	8.179	8.439	1.355	400.9 ^{+5.4} _{-5.3}	–	α ² CVn
V819 Cyg	10618721	K0	6.381	8.625	1.291	262.8 ^{+1.7} _{-1.6}	–	SPB

constrain fundamental stellar parameters as through these scaling relations:

$$\nu_{\max} \propto \frac{g}{g_{\odot}} \cdot \left(\frac{T_{\text{eff}}}{T_{\text{eff}\odot}} \right)^{\frac{1}{2}} \quad (1)$$

and

$$\langle \Delta \nu \rangle \propto \sqrt{\langle \rho \rangle} = \sqrt{\frac{M}{M_{\odot}} \left(\frac{R}{R_{\odot}} \right)^{-3}} \quad (2)$$

We have followed the method of [Davies & Miglio \(2016\)](#), obtaining a Lomb-Scargle periodogram of the smoothed time se-

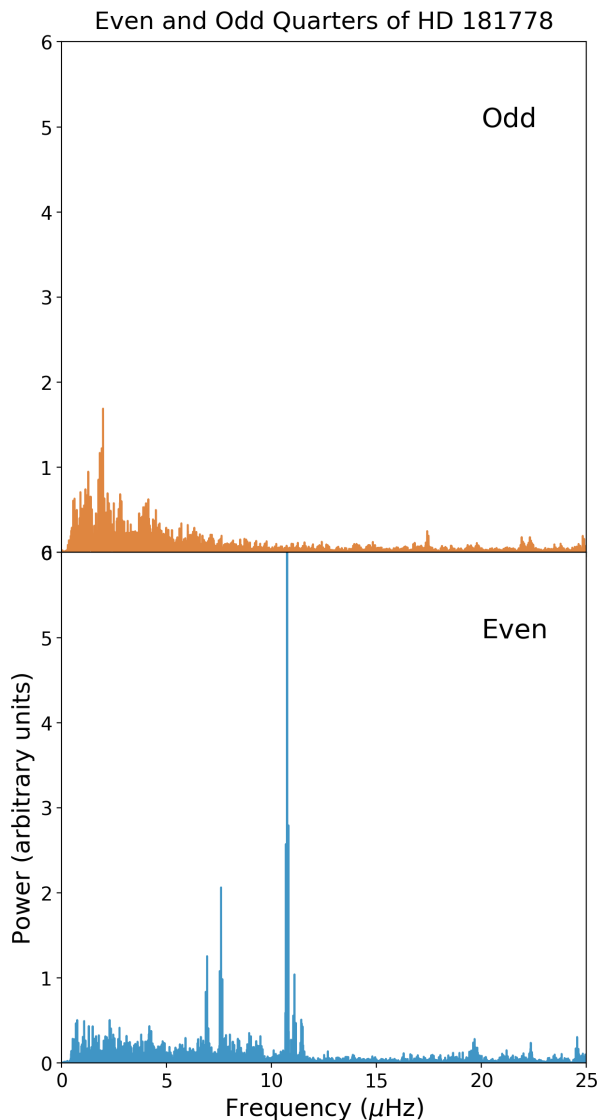


Figure 3. Power spectra of odd and even quarters of HD 181778. It is clear from inspection that while odd quarters have the power spectrum expected of a giant star, even quarters have very high amplitude coherent oscillations typical of an M giant.

ries according to the method of [García et al. \(2011\)](#). The posterior distribution of the asteroseismic parameters is obtained with a Markov Chain Monte Carlo fit to the smoothed periodogram, applying the combined granulation and oscillation model of [Kallinger et al. \(2014\)](#). This consists of two Harvey profiles for the granulation ([Harvey 1985](#)), a Gaussian envelope for the stellar oscillations, and a white noise background for instrumental noise. The marginal posterior distribution for the oscillation envelope is well-approximated by a single Gaussian, and we have taken its median and standard deviation to be our estimates for ν_{\max} and its uncertainty.

To estimate $\Delta\nu$, we have divided the power spectrum through by the granulation and noise models to obtain a signal-to-noise spectrum, and fit a sum of Lorentzians separated by mean large ($\Delta\nu$) and small ($\delta\nu$) separations to the part of this spectrum in the vicinity of ν_{\max} . In practice, for this dataset, $\delta\nu$ is poorly constrained, but mean $\langle\Delta\nu\rangle$ is typically well-constrained and its posterior marginal distribution is well-represented by a single Gaussian as with ν_{\max} .

We obtain good estimates of these asteroseismic parameters for 34 targets, presented in Table 2. In the remainder of cases, as noted above, we find that the very-low-frequency ($\lesssim 2\mu\text{Hz}$) oscillations are affected by filter artefacts from detrending, and we are not able to obtain good estimates for these stars.

Once ν_{\max} has been estimated, we have used the asteroseismic scaling relation for ν_{\max} (Equation 1; [Kjeldsen & Bedding 1995](#)) to estimate $\log g$ in order to inform extraction of chemical abundances from spectra. Using the initial spectroscopic estimate of T_{eff} , which is not significantly informed by ν_{\max} , uncertainties in ν_{\max} are propagated with Monte Carlo sampling.

For eight stars, we have found that the asteroseismic fit is unsatisfactory: for BD+39 388 we cannot detect the expected oscillations; for BD+43 3064 there are significant peaks but these are not consistent with the pattern expected from a red giant; for HD 179959 and HD 187217 we suspect contamination with the oscillations of a second giant, which is hard to remove from smear light curves; while for HD 188629, HD 188639 and HD 188875 we can extract a ν_{\max} but not a robust $\Delta\nu$. One star in our sample, the retired A star HD 185351, has a mode envelope that is not well fit by our model. The smear light curve for this star has already been published by [Hjørringgaard et al. \(2017\)](#), who showed with detailed asteroseismic modelling that it had a zero-age main sequence mass of $\sim 1.60M_{\odot}$ and used it to calibrate the convective overshoot parameter for low-luminosity red giants. The bulk asteroseismic modelling presented here should therefore be considered to be superseded by the more detailed model of [Hjørringgaard et al. \(2017\)](#).

2.4 Spectroscopy

For the whole red giant sample, we have obtained high-resolution spectroscopy with TRES in order to constrain stellar parameters and elemental abundances. Operating with spectral resolving power $R = 44000$, we have obtained spectra with signal-to-noise ratios (SNRs) of tens to hundreds per resolution element. This resolution and SNR are sufficient for an exploratory study, but for more detailed analysis it will be desirable to use APOGEE or similar instruments to obtain greater spectral coverage. From this observing run we have 34 unique targets with seismic $\log g$ and spectra, one more star than the *Gaia*-ESO benchmark set and a significant addition to the ensemble of bright red giants with asteroseismic parameter determinations. Due to observing constraints, we were unable to obtain spectra for BD+42 3150, BD+48 2904, HD 176209, HD 182354, HD 189636AB, or HD 189750.

To derive stellar parameters from our TRES spectra, we initially ran the Stellar Parameter Classification (SPC; [Buchhave et al. 2012](#)) code to determine T_{eff} and $\log g$, using the SPC T_{eff} to inform the asteroseismic estimation of $\log g$ from ν_{\max} . For deriving abundances, T_{eff} is fixed from the results of an initial SPC fit, while $\log g$ is fixed to the seismic values. The other stellar atmospheric parameters including the microturbulent velocity (v_{mic}), and broadening (convolution by V_{mac} , $v_{\text{sin } i}$ and the instrumental line profile) as well as [Fe/H] and chemical abundances for 20 chemical species are derived using the Brussels Automatic Code for Characterizing High accuracy Spectra (BACCHUS; [Masseron et al. 2016](#)), and the results from this calculation are displayed in Table 3. BACCHUS uses an interpolation scheme through a grid of MARCS model atmospheres ([Gustafsson et al. 2008](#)) in combination with TURBOSPECTRUM ([Alvarez & Plez 1998](#); [Plez 2012](#)). For the calculation of synthetic spectra, atomic line information has been taken from the fifth version of the *Gaia*-ESO linelist ([Heiter et al.](#), in preparation). Additionally we used the molecular species for CH

Table 2. Bulk asteroseismic parameters $\Delta\nu$, ν_{\max} , and ϵ for the red giant sample as discussed in Section 2.3.

Object	$\Delta\nu$ (μHz)	ν_{\max} (μHz)	ϵ
BD+36 3564	0.95 ± 0.03	5.08 ± 0.10	0.83 ± 0.20
BD+39 3577	1.68 ± 0.01	13.27 ± 0.32	0.74 ± 0.06
BD+42 3150	4.22 ± 0.03	38.32 ± 0.96	0.70 ± 0.07
BD+43 3171	0.42 ± 0.05	1.98 ± 0.05	0.80 ± 0.17
BD+43 3213	0.49 ± 0.01	2.56 ± 0.06	1.01 ± 0.07
BD+48 2904	2.85 ± 0.01	23.13 ± 0.72	0.86 ± 0.08
BD+48 2955	0.90 ± 0.01	5.44 ± 0.08	0.81 ± 0.05
HD 174020	0.56 ± 0.02	2.48 ± 0.10	0.89 ± 0.08
HD 174829	1.28 ± 0.01	7.95 ± 0.16	0.78 ± 0.06
HD 175740	5.93 ± 0.01	64.33 ± 0.78	1.00 ± 0.02
HD 175884	1.12 ± 0.01	7.07 ± 0.11	0.96 ± 0.08
HD 176209	4.22 ± 0.08	36.08 ± 0.77	0.87 ± 0.06
HD 178797	1.03 ± 0.02	6.34 ± 0.09	0.74 ± 0.29
HD 178910	3.64 ± 0.02	32.06 ± 0.31	0.83 ± 0.05
HD 179396	3.76 ± 0.02	31.02 ± 0.44	0.92 ± 0.03
HD 180312	4.17 ± 0.02	33.84 ± 0.28	0.96 ± 0.04
HD 180475	0.82 ± 0.00	4.34 ± 0.10	0.68 ± 0.03
HD 180658	4.00 ± 0.02	33.76 ± 0.50	0.90 ± 0.05
HD 180682	0.77 ± 0.05	3.68 ± 0.08	1.07 ± 0.15
HD 181022	0.38 ± 0.01	1.58 ± 0.03	0.70 ± 0.10
HD 181069	4.43 ± 0.01	41.46 ± 0.32	0.90 ± 0.02
HD 181097	1.61 ± 0.02	11.16 ± 0.14	0.72 ± 0.36
HD 181597	3.11 ± 0.01	25.84 ± 0.25	0.97 ± 0.02
HD 181778	2.56 ± 0.02	22.86 ± 0.29	0.72 ± 0.06
HD 181880	1.04 ± 0.01	6.54 ± 0.10	0.76 ± 0.05
HD 182354	2.66 ± 0.01	24.73 ± 0.37	0.74 ± 0.04
HD 182531	1.03 ± 0.00	6.47 ± 0.09	0.86 ± 0.03
HD 182692	4.66 ± 0.01	44.38 ± 0.47	0.87 ± 0.02
HD 182694	5.71 ± 0.01	69.78 ± 1.02	0.94 ± 0.25
HD 183124	4.39 ± 0.01	39.59 ± 0.29	0.95 ± 0.03
HD 185286	0.72 ± 0.01	4.23 ± 0.10	0.73 ± 0.08
HD 188537	1.55 ± 0.01	13.40 ± 0.34	0.72 ± 0.07
HD 189636	2.91 ± 0.01	25.97 ± 0.74	0.97 ± 0.04
HD 189750	4.16 ± 0.04	36.14 ± 0.58	0.94 ± 0.08
HD 226754	1.19 ± 0.01	7.41 ± 0.19	0.74 ± 0.08

(Masseron et al. 2014), CN, NH, OH, MgH C₂ (T. Masseron, private communication). The SiH molecular information is adopted from the Kurucz linelists and the information for TiO, ZrO, FeH, CaH from B. Plez (private communication).

Individual elemental abundances are derived by first fixing the stellar atmospheric parameters to those determined above. Spectra are then synthesized in regions centered around an absorption feature of the element we want to derive. The spectra generated will have different [X/Fe] values. A χ^2 minimization procedure is then done to derive the best fitting abundance for each line. The reported abundances are the median [X/Fe] value of the various line regions for a given element. **Ben: Maybe remove this if we do not actually implement line-by-line differential; Do we have a TRES Arcturus spectrum.** Abundance uncertainties reported are the standard error in the line-by-line abundance ratios. Where only one line exists for a given element, we conservatively assume the standard error is 0.10 dex. In principle, these uncertainties are underestimated because there they do not include the errors driven by imperfect stellar parameter values and other systematic errors arising, for instance, from incorrect line list data. We do note, however, thus use of asteroseismology really reduces the uncertainties caused by the stellar parameters (see Hawkins et al. 2016c, for a

longer discussion on this). To achieve the most precise abundances we have derived them using both with and without a line-by-line differential approach with respect to Arcturus (α Boötis) using the method described by Jofré et al. (2015) and the Arcturus abundances from (Hawkins et al. 2016c). The results of these absolute abundance calculations **without the line-by-line differential analysis implemented?**, are presented in Tables 4, 5 and 6. Because for most elements Arcturus differential abundances are not available, these are provided as supplementary online-only material. No abundances for oxygen could be reliably derived for any of the stars in our spectroscopic sample by either method.

3 RESULTS

3.1 Red Giants

3.1.1 Chemical Composition

The chemical compositions for each star were measured in the α (Mg, Ti, Si, Ca), odd-Z (Al, Na, Cu, Sc, V), Fe-peak (Fe, Ni, Zn, Co, Cr, Mn), and neutron capture (Sr, Y, Zr, Ba, La, Nd, Eu) elemental families. This was done to assess the Galactic populations from which these stars are drawn. The first thing to note is that the metallicities, which are tabulated in Table 3, are too high (with $-0.51 < [\text{M}/\text{H}] < +0.14$ dex) to be considered drawn from the Galactic halo, whose peak metallicity is around ~ -1.50 (e.g. Chiba & Beers 2000). Furthermore, the distance distribution, noted in Table 1, indicates that all stars are located within a few kpc of the Sun and thus are not apart of the Galactic bulge. These alone allow us to predict that these stars are drawn from only the Galactic thick and thin disks. We provide a detailed chemical abundance analysis below to support this claim.

α elements:

The α elements are thought to form in variety ways during internal fusion within a star while it evolves over its life. These elements are then largely dispersed into the interstellar medium through Type II supernovae (SNII) (Matteucci & Recchi 2001). The most important of these diagrams are those including the abundances of the α elements as a function of metallicity. It has been shown by many studies (e.g. Edvardsson et al. 1993; Adibekyan et al. 2012; Feltzing & Chiba 2013; Bensby et al. 2014, and references therein), that the Galactic thick disk and thin disk separate in the α elements, where the thick disk is enhanced in [Mg, Si, Ca, Ti/Fe] compared to the Galactic thin disk at a given metallicity. In Fig. 4, we display the [Mg, Si, Ca, Ti/Fe] abundance ratios as a function of [Fe/H] for our stars (black circles) compared¹ to representative disk stars from (open red square, Bensby et al. 2014) and (open orange triangles, Adibekyan et al. 2012).

For most of the stars in our sample, the [Mg, Ti, Ca/Fe] abundance ratios are enhanced. The commonly used $[\alpha/\text{Fe}]$ abundance ratio is the average of Mg, Ti, Si, Ca (thus it is $([\text{Mg}/\text{Fe}] + [\text{Ca}/\text{Fe}] + [\text{Si}/\text{Fe}] + [\text{Ti}/\text{Fe}]/4.0)$) is also enhanced in most stars. This is consistent with most stars belonging to the Galactic thick disk. Though there are a handful of stars where the typical $[\alpha/\text{Fe}]$ ratio is solar.

Odd-Z elements:

The odd-Z elements Na and Al are also shown in Fig. 4. These elements are significantly enhanced

¹ We note that there are likely systematics between our [X/Fe] abundance scale and those of our comparison samples. We do not have the relevant data, which include several stars in common with these studies but observed with the TRES spectrograph, to assess the level of systematics.

Table 3. Fundamental stellar parameters for the red giant sample as determined jointly by asteroseismology (asteroseismic $\log g$; Section 2.3) and spectroscopy (RV, T_{eff} , $\log g$, $[M/H]$, $V \sin i$, and SNR; Section 2.4.)

Object	RV (km/s)	T_{eff} (K)	$\log g$	$[M/H]$	$V \sin i$ (km/s)	SNR
BD+36 3564	-77.84 ± 0.05	4301 ± 50	1.58 ± 0.01	-0.34 ± 0.08	5.14 ± 0.50	71.8
BD+39 3577	-14.81 ± 0.07	5079 ± 50	2.03 ± 0.01	-0.11 ± 0.08	3.98 ± 0.50	92.8
BD+43 3171	-16.32 ± 0.11	4072 ± 50	1.16 ± 0.01	-0.17 ± 0.08	5.68 ± 0.50	68.6
BD+43 3213	-14.16 ± 0.16	4131 ± 50	1.27 ± 0.01	0.07 ± 0.08	6.24 ± 0.50	57.3
BD+48 2955	1.66 ± 0.04	4344 ± 50	1.61 ± 0.01	-0.32 ± 0.08	4.78 ± 0.50	31.7
HD 174020	-14.84 ± 0.08	4162 ± 50	1.26 ± 0.02	-0.10 ± 0.08	5.81 ± 0.50	120.1
HD 174829	10.15 ± 0.03	4482 ± 50	1.78 ± 0.01	-0.40 ± 0.08	4.41 ± 0.50	112.2
HD 175740	-8.82 ± 0.05	4973 ± 50	2.71 ± 0.01	-0.05 ± 0.08	3.66 ± 0.50	264.0
HD 175740	-8.82 ± 0.05	4973 ± 50	2.71 ± 0.01	-0.05 ± 0.08	3.66 ± 0.50	264.0
HD 175740	-8.82 ± 0.05	4973 ± 50	2.71 ± 0.01	-0.05 ± 0.08	3.66 ± 0.50	264.0
HD 175740	-8.82 ± 0.05	4973 ± 50	2.71 ± 0.01	-0.05 ± 0.08	3.66 ± 0.50	264.0
HD 175740	-8.82 ± 0.05	4973 ± 50	2.71 ± 0.01	-0.05 ± 0.08	3.66 ± 0.50	264.0
HD 175884	-34.39 ± 0.07	4466 ± 50	1.73 ± 0.01	-0.27 ± 0.08	4.46 ± 0.50	144.4
HD 178797	6.35 ± 0.05	4406 ± 50	1.68 ± 0.01	-0.37 ± 0.08	4.18 ± 0.50	77.1
HD 178910	-14.28 ± 0.05	4589 ± 50	2.39 ± 0.00	0.14 ± 0.08	4.26 ± 0.50	76.9
HD 179396	24.80 ± 0.04	4781 ± 50	2.39 ± 0.01	-0.21 ± 0.08	3.99 ± 0.50	82.7
HD 180312	-21.94 ± 0.05	4916 ± 50	2.43 ± 0.00	-0.44 ± 0.08	4.05 ± 0.50	73.5
HD 180312	-21.94 ± 0.05	4916 ± 50	2.43 ± 0.00	-0.44 ± 0.08	4.05 ± 0.50	73.5
HD 180475	-45.90 ± 0.08	4398 ± 50	1.52 ± 0.01	-0.44 ± 0.08	4.39 ± 0.50	58.4
HD 180658	2.97 ± 0.06	4802 ± 50	2.43 ± 0.01	-0.12 ± 0.08	3.81 ± 0.50	72.3
HD 180682	30.99 ± 0.07	4410 ± 50	1.45 ± 0.01	-0.51 ± 0.08	4.88 ± 0.50	80.1
HD 181022	-80.39 ± 0.16	4045 ± 50	1.06 ± 0.01	-0.28 ± 0.08	5.75 ± 0.50	108.8
HD 181069	9.99 ± 0.05	4842 ± 50	2.52 ± 0.00	-0.05 ± 0.08	3.53 ± 0.50	90.0
HD 181097	-5.60 ± 0.08	4520 ± 50	1.93 ± 0.01	-0.28 ± 0.08	4.08 ± 0.50	69.7
HD 181597	-13.06 ± 0.04	4751 ± 50	2.31 ± 0.00	-0.23 ± 0.08	2.23 ± 0.50	161.8
HD 181778	-22.04 ± 0.06	4664 ± 50	2.25 ± 0.01	-0.19 ± 0.08	4.23 ± 0.50	87.6
HD 181880	0.56 ± 0.08	4405 ± 50	1.70 ± 0.01	-0.30 ± 0.08	4.44 ± 0.50	71.2
HD 182531	-7.34 ± 0.05	4413 ± 50	1.69 ± 0.01	-0.24 ± 0.08	4.39 ± 0.50	71.4
HD 182692	-8.01 ± 0.05	4965 ± 50	2.55 ± 0.00	0.09 ± 0.08	3.40 ± 0.50	72.8
HD 182694	-0.87 ± 0.06	5178 ± 50	2.76 ± 0.01	-0.12 ± 0.08	5.12 ± 0.50	187.2
HD 183124	14.96 ± 0.01	4911 ± 50	2.50 ± 0.00	-0.15 ± 0.08	5.19 ± 0.50	114.3
HD 185286	-13.70 ± 0.08	4301 ± 50	1.50 ± 0.01	-0.14 ± 0.08	5.16 ± 0.50	135.6
HD 188537	-18.03 ± 0.15	4961 ± 50	2.03 ± 0.01	-0.08 ± 0.08	10.68 ± 0.50	67.0
HD 226754	18.66 ± 0.10	4370 ± 50	1.75 ± 0.01	0.08 ± 0.08	4.78 ± 0.50	62.5

Fe-peak elements:

XX

Neutron capture elements:

XX

Two of the stars in our sample also appear in the Hypatia catalogue of stellar abundances (Hinkel et al. 2014): HD 185351 and HD 175740. The abundances reported here for HD 185351 are consistent within the large errorbars of both surveys with those reported in Hypatia, while for HD 175740 they are not. **Keith - what's going on here? Check this?**

3.1.2 Red Clump Stars

Red clump stars, which burn helium in their cores, differ significantly in their core structure from stars on the hydrogen shell burning red giant sequence. They can therefore be distinguished from hydrogen-shell burning giants asteroseismologically, due to their much higher g -mode period spacings (Bedding et al. 2011). The moniker ‘red clump’ arises from the fact that such stars can have a very narrow range of luminosities, so that they appear as a clump in the HR diagram (Girardi 2016). This property makes them useful standard candles to which distances can be accurately computed from photometry. Red clump stars have been used to calibrate

the *Gaia* survey’s parallaxes at long distances (Davies et al. 2017; Hawkins et al. 2017; Ruiz-Dern et al. 2018). *Gaia* DR2 parallaxes have a zero-point offset of ~ 0.03 mas (Lindgren et al. 2018), and in particular hierarchical models of the ensemble of *Gaia* clump stars can be used to accurately estimate this and thereby improve the accuracy of *Gaia* distances greater than a few kpc (Hawkins et al., in prep.).

From visual inspection of the power spectra, HD 181069, HD 183124, HD 182354, HD 182692, and HD 180658 are seen to be red clump stars. A power spectrum of the best example of these, HD 183124, together with an échelle diagram used to estimate its g -mode period spacing, is shown in Figure 5. While precise characterization of these stars to the necessary degree is beyond the scope of this paper, they are ideal candidates for anchoring models of the mass and metallicity dependence of red clump properties for calibrating *Gaia* and other distance measures.

3.1.3 Long Period Variables**3.2 Main Sequence Stars**

For all the main sequence stars in our sample, we visually inspected light curves and power spectra to determine their variability class.

Table 4. Chemical abundances relative to iron for stars in the red giant sample as determined by BACCHUS, without differential line-by-line comparison to Arcturus, as described in Section 2.4, for the elements Ca, Mg, Si, Ti, Al, Ba, and Na. Dashes indicate elements for which abundances could not be reliably computed. The catalogue of abundances for more elements continues in Tables 5 and 6.

Object	[Ca/Fe]	[Mg/Fe]	[Si/Fe]	[Ti/Fe]	[Al/Fe]	[Ba/Fe]	[Na/Fe]
BD+36 3564	0.21 ± 0.02	0.33 ± 0.03	0.10 ± 0.03	0.34 ± 0.04	0.40 ± 0.01	–	0.26 ± 0.08
BD+39 3577	0.13 ± 0.02	0.22 ± 0.04	−0.11 ± 0.02	0.08 ± 0.04	0.21 ± 0.01	0.35 ± 0.10	0.42 ± 0.00
BD+43 3064	0.19 ± 0.04	0.21 ± 0.03	−0.01 ± 0.03	0.28 ± 0.04	0.36 ± 0.01	–	0.48 ± 0.06
BD+43 3171	0.29 ± 0.03	0.26 ± 0.06	−0.00 ± 0.07	0.21 ± 0.06	0.42 ± 0.01	0.33 ± 0.18	0.18 ± 0.25
BD+43 3213	0.19 ± 0.03	0.23 ± 0.07	−0.18 ± 0.11	0.27 ± 0.07	0.37 ± 0.04	–	0.62 ± 0.37
BD+48 2955	0.22 ± 0.05	0.20 ± 0.03	0.08 ± 0.04	0.30 ± 0.04	0.30 ± 0.07	–	0.23 ± 0.14
HD 174020	0.33 ± 0.03	0.23 ± 0.04	−0.07 ± 0.06	0.29 ± 0.07	0.39 ± 0.03	–	0.26 ± 0.33
HD 174829	0.16 ± 0.04	0.20 ± 0.06	0.05 ± 0.05	0.19 ± 0.03	0.29 ± 0.01	–	0.31 ± 0.04
HD 175740	0.12 ± 0.02	0.07 ± 0.05	−0.05 ± 0.02	0.14 ± 0.03	0.21 ± 0.01	0.30 ± 0.07	0.34 ± 0.03
HD 175884	0.23 ± 0.02	0.20 ± 0.03	−0.01 ± 0.03	0.32 ± 0.03	0.34 ± 0.01	–	0.46 ± 0.06
HD 178797	0.22 ± 0.02	0.32 ± 0.03	0.06 ± 0.03	0.40 ± 0.04	0.42 ± 0.01	0.39 ± 0.22	0.45 ± 0.03
HD 178910	0.20 ± 0.03	0.20 ± 0.03	0.15 ± 0.05	0.20 ± 0.03	0.39 ± 0.04	0.25 ± 0.08	0.36 ± 0.98
HD 179396	0.09 ± 0.02	0.19 ± 0.03	0.04 ± 0.05	0.13 ± 0.02	0.27 ± 0.02	0.31 ± 0.03	0.28 ± 0.04
HD 179959	0.04 ± 0.04	0.06 ± 0.04	0.01 ± 0.03	0.03 ± 0.03	0.15 ± 0.02	–	0.38 ± 0.02
HD 180312	0.09 ± 0.02	0.21 ± 0.03	0.06 ± 0.03	0.09 ± 0.03	0.31 ± 0.01	0.37 ± 0.08	0.19 ± 0.01
HD 180475	0.23 ± 0.03	0.33 ± 0.03	0.03 ± 0.01	0.36 ± 0.04	0.41 ± 0.02	0.30 ± 0.20	0.40 ± 0.03
HD 180658	0.15 ± 0.03	0.19 ± 0.04	−0.01 ± 0.03	0.21 ± 0.03	0.35 ± 0.01	0.21 ± 0.09	0.39 ± 0.04
HD 180682	0.25 ± 0.02	0.45 ± 0.03	0.13 ± 0.02	0.47 ± 0.04	0.51 ± 0.05	0.19 ± 0.05	0.32 ± 0.01
HD 181022	0.34 ± 0.02	0.34 ± 0.06	0.01 ± 0.08	0.49 ± 0.06	–	0.31 ± 0.23	0.09 ± 0.48
HD 181069	0.13 ± 0.02	0.17 ± 0.04	−0.03 ± 0.05	0.19 ± 0.03	0.28 ± 0.02	0.26 ± 0.09	0.45 ± 0.06
HD 181097	0.25 ± 0.02	0.27 ± 0.03	−0.02 ± 0.03	0.35 ± 0.03	0.34 ± 0.02	–	0.46 ± 0.06
HD 181597	0.19 ± 0.02	0.20 ± 0.05	−0.03 ± 0.02	0.27 ± 0.04	0.28 ± 0.00	0.28 ± 0.05	0.42 ± 0.04
HD 181778	0.06 ± 0.03	0.12 ± 0.03	0.00 ± 0.03	0.09 ± 0.03	0.28 ± 0.02	0.47 ± 0.05	0.42 ± 0.12
HD 181880	0.26 ± 0.02	0.30 ± 0.03	0.06 ± 0.04	0.35 ± 0.03	0.42 ± 0.01	–	0.40 ± 0.05
HD 182531	0.22 ± 0.02	0.21 ± 0.05	−0.07 ± 0.03	0.37 ± 0.04	0.39 ± 0.01	–	0.48 ± 0.06
HD 182692	0.19 ± 0.03	0.18 ± 0.04	−0.12 ± 0.03	0.22 ± 0.04	0.35 ± 0.03	0.13 ± 0.05	0.38 ± 0.12
HD 182694	0.10 ± 0.02	0.11 ± 0.04	−0.04 ± 0.02	0.05 ± 0.02	0.14 ± 0.01	–	0.32 ± 0.01
HD 183124	0.17 ± 0.02	0.21 ± 0.04	−0.02 ± 0.04	0.19 ± 0.03	0.29 ± 0.00	0.25 ± 0.05	0.35 ± 0.02
HD 185286	0.34 ± 0.02	0.22 ± 0.04	−0.04 ± 0.04	0.40 ± 0.06	0.42 ± 0.02	–	0.55 ± 0.53
HD 185351	0.13 ± 0.03	0.08 ± 0.05	−0.08 ± 0.02	0.20 ± 0.03	0.22 ± 0.00	0.21 ± 0.09	0.38 ± 0.01
HD 187217	0.16 ± 0.04	0.28 ± 0.02	−0.09 ± 0.03	0.14 ± 0.04	0.32 ± 0.03	0.21 ± 0.14	–
HD 188537	0.11 ± 0.04	0.27 ± 0.04	0.02 ± 0.03	0.11 ± 0.04	0.25 ± 0.05	0.24 ± 0.07	–
HD 188629	0.30 ± 0.03	0.21 ± 0.03	−0.04 ± 0.07	0.37 ± 0.07	0.41 ± 0.04	–	0.46 ± 0.32
HD 188875	0.18 ± 0.04	0.22 ± 0.03	−0.07 ± 0.03	0.29 ± 0.04	0.33 ± 0.02	–	0.61 ± 1.09
HD 226754	0.30 ± 0.02	0.31 ± 0.04	0.03 ± 0.04	0.40 ± 0.06	0.48 ± 0.07	0.43 ± 0.00	0.47 ± 0.18

In the following subsections, we will briefly comment on some of the findings. As main sequence variables are so diverse, and suited to varied science cases, we have attempted only a very preliminary study of these stars in this paper, leaving detailed analysis to future work.

3.2.1 Classical Pulsators

The sample contains many δ Sct and γ Dor variables, and several hybrid pulsators. [Simon - add text here](#). Including hotter stars, we also detect SPB pulsations in [some stars - Conny/Tim van Reeth?](#).

3.2.2 Hump and Spike Stars

Two stars in the sample show the ‘hump-and-spike’ morphology in their power spectra (a broad ‘hump’ of low-amplitude oscillations dominated by one high amplitude coherent oscillation toward the high frequency end of this band): HD 186155 (HR 7495), and HD 183362 (HR 7403), respectively the third brightest and 37th-brightest stars on silicon and the brightest two stars that show this effect. [Saio et al. \(2018\)](#) have recently claimed the hump-and-spike power spectra as evidence for Rossby modes. The F5

star HD 186155, identified by SIMBAD as having a giant spectral type of F5II-III, is shown by its *Gaia* distance to in fact lie on the main sequence. The other example is the B3e star HD 183362 at $G = -2.576$. A detailed study of these stars will be presented by Antoci et al., in prep.

Another star with a hump-and-spike spectrum is Boyajian’s Star, which shows deep enigmatic dips in brightness ([Boyajian et al. 2016](#)), and has faded both throughout the *Kepler* mission ([Montet & Simon 2016](#)) and in relation to Harvard photographic plates from 1890 onwards ([Schaefer 2016](#)). The dimming, which is chromatic in the manner expected of heterogeneous clouds of circumstellar dust in the line of sight ([Davenport et al. 2018](#); [Bodman et al. 2018](#)), has been ascribed to various causes (reviewed in [Wright 2018](#)), most notably a cloud of exocomets surrounding the star (e.g. [Wyatt et al. 2018](#)). It is unclear whether the explanation of the hump-and-spike phenomenon will shed light on the strange behaviour of Boyajian’s Star, but it may be relevant.

[Ashley/Dan/Vichi?](#)

3.2.3 Eclipsing Binaries

We detect some eclipsing binaries [Ben - finish this](#).

Table 5. Chemical abundances relative to iron for stars in the red giant sample as determined by BACCHUS, without differential line-by-line comparison to Arcturus, as described in Section 2.4, for the elements Ni, Mn, Co, Eu, La, Zr, and Sr. Dashes indicate elements for which abundances could not be reliably computed. The catalogue of abundances for more elements continues in Table 6.

Object	[Ni/Fe]	[Mn/Fe]	[Co/Fe]	[Eu/Fe]	[La/Fe]	[Zr/Fe]	[Sr/Fe]
BD+36 3564	0.01 ± 0.04	0.08 ± 0.00	0.13 ± 0.02	0.25 ± 0.03	−0.02 ± 0.07	0.10 ± 0.02	0.34 ± 0.12
BD+39 3577	−0.05 ± 0.03	−0.03 ± 0.06	−0.02 ± 0.02	−0.22 ± 0.04	−0.25 ± 0.02	0.13 ± 0.08	–
BD+43 3064	0.05 ± 0.04	0.21 ± 0.02	0.13 ± 0.02	0.28 ± 0.06	0.15 ± 0.02	0.32 ± 0.04	0.25 ± 0.12
BD+43 3171	0.04 ± 0.05	0.11 ± 0.09	0.14 ± 0.05	0.21 ± 0.05	−0.06 ± 0.11	0.36 ± 0.07	–
BD+43 3213	0.06 ± 0.10	0.33 ± 0.07	0.03 ± 0.05	0.06 ± 0.04	−0.11 ± 0.05	0.49 ± 0.11	0.64 ± 0.47
BD+48 2955	0.05 ± 0.04	0.10 ± 0.02	0.12 ± 0.04	0.28 ± 0.04	0.24 ± 0.05	0.34 ± 0.05	–
HD 174020	0.05 ± 0.05	0.23 ± 0.02	0.10 ± 0.04	0.11 ± 0.04	0.02 ± 0.07	–	0.37 ± 0.89
HD 174829	−0.06 ± 0.04	−0.02 ± 0.07	0.05 ± 0.02	0.15 ± 0.01	0.12 ± 0.05	0.08 ± 0.03	–
HD 175740	0.03 ± 0.04	0.06 ± 0.01	0.08 ± 0.02	0.09 ± 0.07	0.12 ± 0.01	0.18 ± 0.02	–
HD 175884	0.04 ± 0.05	0.14 ± 0.02	0.10 ± 0.02	0.19 ± 0.02	0.14 ± 0.03	0.26 ± 0.02	–
HD 178797	0.05 ± 0.04	0.13 ± 0.11	0.18 ± 0.03	0.26 ± 0.02	0.14 ± 0.02	0.23 ± 0.03	–
HD 178910	0.28 ± 0.07	0.21 ± 0.05	0.17 ± 0.03	−0.02 ± 0.06	−0.13 ± 0.06	0.00 ± 0.03	–
HD 179396	−0.02 ± 0.04	0.09 ± 0.02	0.08 ± 0.03	−0.05 ± 0.03	0.05 ± 0.03	0.04 ± 0.02	–
HD 179959	−0.08 ± 0.04	−0.15 ± 0.04	−0.05 ± 0.02	0.16 ± 0.06	0.18 ± 0.01	0.14 ± 0.07	–
HD 180312	0.02 ± 0.03	−0.09 ± 0.03	0.07 ± 0.01	0.34 ± 0.05	0.04 ± 0.07	0.08 ± 0.02	–
HD 180475	0.03 ± 0.05	0.16 ± 0.04	0.19 ± 0.02	0.19 ± 0.07	0.18 ± 0.03	0.25 ± 0.03	–
HD 180658	0.03 ± 0.06	0.13 ± 0.03	0.11 ± 0.02	–	0.04 ± 0.04	0.16 ± 0.07	–
HD 180682	0.06 ± 0.04	−0.03 ± 0.08	0.20 ± 0.02	0.26 ± 0.03	−0.03 ± 0.02	0.22 ± 0.03	–
HD 181022	0.02 ± 0.07	0.05 ± 0.11	0.14 ± 0.05	0.26 ± 0.03	−0.03 ± 0.21	0.36 ± 0.14	–
HD 181069	0.08 ± 0.05	0.16 ± 0.03	0.12 ± 0.02	0.09 ± 0.03	0.02 ± 0.04	0.10 ± 0.03	–
HD 181097	0.01 ± 0.04	0.02 ± 0.11	0.14 ± 0.03	0.28 ± 0.04	0.17 ± 0.02	0.23 ± 0.03	–
HD 181597	0.03 ± 0.04	0.14 ± 0.01	0.13 ± 0.02	0.18 ± 0.03	0.13 ± 0.01	0.26 ± 0.03	–
HD 181778	−0.00 ± 0.05	0.13 ± 0.02	0.04 ± 0.02	0.16 ± 0.01	0.08 ± 0.03	0.11 ± 0.03	–
HD 181880	0.04 ± 0.04	0.10 ± 0.01	0.18 ± 0.03	0.32 ± 0.04	0.17 ± 0.02	0.33 ± 0.04	–
HD 182531	0.06 ± 0.04	0.17 ± 0.06	0.11 ± 0.02	0.16 ± 0.05	0.15 ± 0.03	0.36 ± 0.03	0.35 ± 0.14
HD 182692	0.03 ± 0.05	0.22 ± 0.02	0.15 ± 0.02	0.01 ± 0.05	0.06 ± 0.04	0.21 ± 0.03	–
HD 182694	−0.07 ± 0.04	−0.08 ± 0.02	0.03 ± 0.03	0.16 ± 0.02	0.16 ± 0.02	0.16 ± 0.04	–
HD 183124	−0.00 ± 0.05	0.01 ± 0.04	0.11 ± 0.02	0.17 ± 0.05	0.04 ± 0.06	0.14 ± 0.04	–
HD 185286	0.12 ± 0.04	0.25 ± 0.01	0.13 ± 0.03	0.18 ± 0.03	0.12 ± 0.05	0.52 ± 0.05	0.30 ± 0.05
HD 185351	0.01 ± 0.04	0.11 ± 0.02	0.15 ± 0.03	−0.06 ± 0.06	0.13 ± 0.03	0.29 ± 0.04	–
HD 187217	−0.03 ± 0.06	−0.10 ± 0.10	−0.03 ± 0.02	–	−0.07 ± 0.03	0.22 ± 0.04	–
HD 188537	0.05 ± 0.07	0.10 ± 0.03	0.12 ± 0.04	0.20 ± 0.04	0.15 ± 0.10	0.30 ± 0.04	–
HD 188629	0.10 ± 0.06	0.22 ± 0.01	0.10 ± 0.02	0.15 ± 0.03	0.06 ± 0.07	0.43 ± 0.01	0.34 ± 0.22
HD 188875	−0.02 ± 0.05	0.23 ± 0.02	0.09 ± 0.03	0.19 ± 0.07	0.20 ± 0.05	0.30 ± 0.03	–
HD 226754	0.19 ± 0.05	0.33 ± 0.03	0.23 ± 0.03	0.28 ± 0.07	−0.05 ± 0.07	0.34 ± 0.04	0.26 ± 0.13

4 OPEN SCIENCE

We believe in open science, and have therefore made all substantive products of this research available to the interested reader. All code used to produce smear light curves is available under a GPL v3 license at github.com/benjaminpope/keplersmear. All smear light curves, both including the red giant sample studied in detail in Section 3.1, and main sequence stars as discussed in Sections 3.2.1 and 3.2.3, can be downloaded from the Mikulski Archive for Space Telescopes (MAST) as a High-Level Science Product. TRES spectra will be made available from the ExoFOP-TESS website, and all asteroseismic parameters and derived stellar parameters for the red giants in Section 3.1 are provided in an online-only table as Supplementary Material to this paper.

All smear light curves in this paper, as well as the L^AT_EX source code used to produce this document, can be found at github.com/benjaminpope/smearcampaign.

5 CONCLUSIONS

The *Kepler* Smear Campaign establishes a legacy sample of 102 very bright stars, with *Kepler* light curves that in almost all cases re-

veal astrophysically interesting variability. The virtue of these bright stars is that they can be studied with interferometry, and more easily with spectroscopy than fainter targets, permitting especially detailed characterization. We have therefore obtained detailed abundances of a subset of the red giants in this sample, particularly with a view to determining their provenance in the Galactic thick and thin disk populations. The science that can be done both with this sample and with this method are, however, considerably broader: while we have not attempted it in this paper, a compelling next step is to use interferometric diameter measurements and to further constrain the red giant parameters, and compare these to the constraints from *Gaia*. Any tension between these measurements will help test and refine the asteroseismic scaling relations, and better models will propagate through to smaller systematic uncertainties in large samples of stars too faint for interferometry. Further improvements will be revealed by the detailed modelling of individual oscillation frequencies in these giants to infer interior structure such as convective overshoot, which is at the time of writing an active topic of research. For the lower-frequency M giants classed as LPVs in this paper, extending the systematics correction and quarter-stitching algorithms to more robustly correct their light curves without removing real signal will

Table 6. Chemical abundances relative to iron for stars in the red giant sample as determined by BACCHUS, without differential line-by-line comparison to Arcturus, as described in Section 2.4, for the elements Zn, Y, Cr, V, Cu, and Sc. Dashes indicate elements for which abundances could not be reliably computed.

Object	[Zn/Fe]	[Y/Fe]	[Cr/Fe]	[V/Fe]	[Cu/Fe]	[Sc/Fe]
BD+36 3564	-0.29 ± 0.20	-0.27 ± 0.02	0.23 ± 0.00	0.15 ± 0.03	-0.04 ± 0.06	0.17 ± 0.02
BD+39 3577	-0.24 ± 0.71	-0.40 ± 0.04	0.16 ± 0.10	0.01 ± 0.02	-0.21 ± 0.01	-0.12 ± 0.05
BD+43 3064	–	-0.14 ± 0.05	0.32 ± 0.01	0.24 ± 0.03	-0.16 ± 0.10	0.14 ± 0.02
BD+43 3171	-0.40 ± 0.05	-0.31 ± 0.03	0.29 ± 0.04	0.12 ± 0.06	0.02 ± 0.11	0.14 ± 0.03
BD+43 3213	–	-0.06 ± 0.09	0.39 ± 0.01	0.08 ± 0.09	-0.28 ± 0.11	0.18 ± 0.04
BD+48 2955	–	-0.15 ± 0.05	0.23 ± 0.04	0.20 ± 0.03	-0.05 ± 0.04	0.15 ± 0.03
HD 174020	-0.48 ± 1.11	-0.19 ± 0.06	0.41 ± 0.06	0.26 ± 0.03	-0.20 ± 0.11	0.18 ± 0.03
HD 174829	-0.12 ± 0.13	-0.25 ± 0.06	0.16 ± 0.02	0.01 ± 0.02	-0.23 ± 0.03	0.12 ± 0.03
HD 175740	-0.16 ± 0.16	-0.09 ± 0.07	0.13 ± 0.04	0.09 ± 0.02	-0.16 ± 0.04	0.08 ± 0.03
HD 175884	-0.15 ± 0.17	-0.21 ± 0.07	0.26 ± 0.04	0.21 ± 0.02	-0.10 ± 0.05	0.13 ± 0.02
HD 178797	–	-0.08 ± 0.05	0.26 ± 0.04	0.19 ± 0.02	-0.11 ± 0.04	0.23 ± 0.03
HD 178910	-0.29 ± 0.74	-0.18 ± 0.05	0.29 ± 0.01	0.17 ± 0.02	0.21 ± 0.14	0.14 ± 0.02
HD 179396	-0.07 ± 0.15	-0.27 ± 0.07	0.12 ± 0.03	0.03 ± 0.02	-0.16 ± 0.06	0.10 ± 0.03
HD 179959	0.05 ± 1.84	-0.08 ± 0.06	-0.00 ± 0.03	-0.11 ± 0.02	-0.29 ± 0.05	0.10 ± 0.05
HD 180312	-0.18 ± 0.01	-0.23 ± 0.05	-0.06 ± 0.06	-0.05 ± 0.02	-0.15 ± 0.04	0.15 ± 0.05
HD 180475	-0.09 ± 0.11	-0.25 ± 0.08	0.24 ± 0.04	0.20 ± 0.02	-0.00 ± 0.04	0.21 ± 0.03
HD 180658	0.16 ± 1.25	-0.20 ± 0.01	0.19 ± 0.04	0.15 ± 0.02	-0.05 ± 0.06	0.12 ± 0.03
HD 180682	-0.23 ± 0.14	-0.29 ± 0.04	0.23 ± 0.03	0.26 ± 0.02	-0.06 ± 0.04	0.27 ± 0.02
HD 181022	-0.27 ± 0.03	-0.23 ± 0.02	0.19 ± 0.08	0.10 ± 0.08	-0.01 ± 0.12	0.25 ± 0.04
HD 181069	-0.02 ± 0.19	-0.11 ± 0.08	0.22 ± 0.03	0.15 ± 0.02	-0.10 ± 0.05	0.13 ± 0.03
HD 181097	-0.08 ± 0.41	-0.21 ± 0.03	0.25 ± 0.02	0.19 ± 0.03	-0.12 ± 0.03	0.22 ± 0.03
HD 181597	-0.14 ± 0.15	-0.19 ± 0.08	0.19 ± 0.05	0.21 ± 0.02	-0.18 ± 0.04	0.16 ± 0.02
HD 181778	-0.03 ± 0.18	-0.13 ± 0.04	0.18 ± 0.02	-0.02 ± 0.02	-0.25 ± 0.07	0.05 ± 0.02
HD 181880	-0.04 ± 0.22	-0.20 ± 0.07	0.27 ± 0.03	0.22 ± 0.02	-0.07 ± 0.03	0.23 ± 0.03
HD 182531	0.03 ± 0.78	-0.19 ± 0.07	0.29 ± 0.05	0.24 ± 0.03	-0.08 ± 0.05	0.18 ± 0.02
HD 182692	-0.24 ± 1.34	-0.21 ± 0.10	0.15 ± 0.07	0.24 ± 0.02	-0.11 ± 0.06	0.18 ± 0.03
HD 182694	-0.24 ± 0.07	-0.12 ± 0.05	0.04 ± 0.03	-0.05 ± 0.02	-0.26 ± 0.04	0.09 ± 0.05
HD 183124	-0.18 ± 0.17	-0.24 ± 0.03	0.12 ± 0.04	0.10 ± 0.02	-0.22 ± 0.02	0.10 ± 0.03
HD 185286	–	-0.19 ± 0.08	0.46 ± 0.01	0.34 ± 0.02	-0.11 ± 0.10	0.27 ± 0.03
HD 185351	-0.31 ± 0.10	-0.16 ± 0.05	0.16 ± 0.04	0.18 ± 0.02	-0.17 ± 0.03	0.12 ± 0.04
HD 187217	–	-0.37 ± 0.05	0.28 ± 0.03	0.11 ± 0.03	-0.23 ± 0.02	0.04 ± 0.05
HD 188537	0.32 ± 0.78	-0.27 ± 0.09	0.17 ± 0.01	0.11 ± 0.02	-0.17 ± 0.04	0.06 ± 0.05
HD 188629	–	-0.04 ± 0.10	0.30 ± 0.06	0.31 ± 0.04	-0.15 ± 0.09	0.22 ± 0.04
HD 188875	0.31 ± 1.71	-0.04 ± 0.07	0.33 ± 0.07	0.18 ± 0.02	-0.25 ± 0.07	0.13 ± 0.03
HD 226754	-0.22 ± 1.07	-0.33 ± 0.04	0.38 ± 0.07	0.45 ± 0.04	-0.02 ± 0.07	0.30 ± 0.04

allow similar asteroseismic analysis, for a sample of stars that are much less well understood than their higher-frequency counterparts.

The *Kepler* Smear Campaign has another natural extension: while many saturated stars in *K2* have now been observed with ‘halo’ apertures including their unsaturated pixels, many were not, either because they were fainter than the typical $Kp \lesssim 6.5$ limit, or because in Campaigns 0-3 and 5 no such apertures were selected. There is therefore the potential for a *K2* Smear Campaign to complete the *K2* sample down to fainter magnitudes, complementing the very brightest stars studied with halo photometry.

ACKNOWLEDGEMENTS

This work was performed in part under contract with the Jet Propulsion Laboratory (JPL) funded by NASA through the Sagan Fellowship Program executed by the NASA Exoplanet Science Institute. B.P. also acknowledges support from Balliol College and the Clarendon Fund. D.H. acknowledges support by the Australian Research Council’s Discovery Projects funding scheme (project number DE140101364) and support by the NASA Grant NNX14AB92G issued through the *Kepler* Participating Scientist Program. DWL acknowledges partial support from the *Kepler* Extended Mission under

NASA Cooperative Agreement NNX13AB58A with the Smithsonian Astrophysical Observatory.

BP acknowledges being on the traditional territory of the Lenape Nations and, today, we recognize that Manhattan continues to be the home to many Algonkian peoples. We thank the Lenape peoples for allowing us to carry out this work on the Lenape original homelands at New York University. BP and TW would like to acknowledge the Gadigal people of the Eora Nation and the Norongerragal and Gweagal peoples of the Tharawal Nation as the traditional owners of the land at the University of Sydney and the Sutherland Shire on which some of this work was carried out, and pay their respects to their knowledge, and their elders past, present and future.

This work has made use of data from the European Space Agency (ESA) mission *Gaia* (<https://www.cosmos.esa.int/gaia>), processed by the *Gaia* Data Processing and Analysis Consortium (DPAC, <https://www.cosmos.esa.int/web/gaia/dpac/consortium>). Funding for the DPAC has been provided by national institutions, in particular the institutions participating in the *Gaia* Multilateral Agreement. This work has in particular made use of the [gaia-kepler.fun](https://github.com/gaia-kepler) crossmatch database created by Megan Bedell.

This research made use of NASA’s Astrophysics Data Sys-



Figure 4. The $[Mg/Fe]$, $[Si/Fe]$, $[Ca/Fe]$, and $[Ti/Fe]$, $[Al/Fe]$, $[Na/Fe]$ abundance ratios as a function of iron on the top and bottom rows, respectively for our stars (black circles). We also illustrate a representative sample of Galactic disk stars from Bensby et al. (open red square, 2014) and Adibekyan et al. (open orange triangles, 2012).



Figure 5. Power spectrum (left) and échelle diagram (right) of the solar-like oscillations of the red clump star HD 183124. The modes in the power spectrum used for the échelle diagram are highlighted with blue dots. In the échelle diagram we see the characteristic pattern of ‘bumped’ modes from avoided crossings between the comb of p -modes and g -mode oscillations with a period spacing of $\Delta\Pi = 300.1$ s.

tem; the SIMBAD database, operated at CDS, Strasbourg, France; the IPython package (Pérez & Granger 2007); SciPy (Jones et al. 2001); and Astropy, a community-developed core Python package for Astronomy (Collaboration et al. 2018). Some of the data presented in this paper were obtained from the Mikulski Archive for Space Telescopes (MAST). STScI is operated by the Association of Universities for Research in Astronomy, Inc., under NASA contract NAS5-26555. Support for MAST for non-HST data is provided by the NASA Office of Space Science via grant NNX13AC07G and by

other grants and contracts. We acknowledge the support of the Group of Eight universities and the German Academic Exchange Service through the Go8 Australia-Germany Joint Research Co-operation Scheme.

REFERENCES

Adibekyan V. Z., Sousa S. G., Santos N. C., Delgado Mena E., González Hernández J. I., Israelian G., Mayor M., Khachatryan G., 2012, *A&A*,

- 545, A32
- Aerts C., et al., 2018, *MNRAS*, 476, 1234
- Aigrain S., Parviainen H., Pope B. J. S., 2016, *MNRAS*, 459, 2408
- Alvarez R., Plez B., 1998, *A&A*, 330, 1109
- Ambikasaran S., Foreman-Mackey D., Greengard L., Hogg D. W., O’Neil M., 2015, *IEEE Transactions on Pattern Analysis and Machine Intelligence*, 38
- Angus R., Aigrain S., Foreman-Mackey D., McQuillan A., 2015, *MNRAS*, 450, 1787
- Bailer-Jones C. A. L., Rybizki J., Fouesneau M., Mantelet G., Andrae R., 2018, preprint, ([arXiv:1804.10121](https://arxiv.org/abs/1804.10121))
- Beck P. G., et al., 2011, *Science*, 332, 205
- Beck P. G., et al., 2012, *Nature*, 481, 55
- Bedding T. R., et al., 2011, *Nature*, 471, 608
- Bensby T., Feltzing S., Oey M. S., 2014, *A&A*, 562, A71
- Blanco-Cuadras S., Soubiran C., Jofré P., Heiter U., 2014, *A&A*, 566, A98
- Bodman E., Wright J., Boyajian T., Ellis T., 2018, preprint, ([arXiv:1806.08842](https://arxiv.org/abs/1806.08842))
- Boyajian T. S., et al., 2016, *MNRAS*, 457, 3988
- Brown T. M., Latham D. W., Everett M. E., Esquerdo G. A., 2011, *AJ*, 142, 112
- Buchhave L. A., et al., 2012, *Nature*, 486, 375
- Campante T. L., et al., 2015, *ApJ*, 799, 170
- Casagrande L., et al., 2014, *MNRAS*, 439, 2060
- Chaplin W. J., Miglio A., 2013, *ARA&A*, 51, 353
- Chaplin W. J., et al., 2010, *ApJ*, 713, L169
- Chiba M., Beers T. C., 2000, *AJ*, 119, 2843
- Christiansen J. L., et al., 2012, *PASP*, 124, 1279
- Collaboration T. A., et al., 2018, *The Astronomical Journal*, 156, 123
- Creevey O. L., et al., 2013, *MNRAS*, 431, 2419
- Creevey O. L., et al., 2015, *A&A*, 575, A26
- Davenport J. R. A., et al., 2018, *ApJ*, 853, 130
- Davies G. R., Miglio A., 2016, *Astronomische Nachrichten*, 337, 774
- Davies G. R., et al., 2017, *A&A*, 598, L4
- Edvardsson B., Andersen J., Gustafsson B., Lambert D. L., Nissen P. E., Tomkin J., 1993, *A&A*, 275, 101
- Farr W. M., et al., 2018, preprint, ([arXiv:1802.09812](https://arxiv.org/abs/1802.09812))
- Feltzing S., Chiba M., 2013, *New Astron. Rev.*, 57, 80
- Gaia Collaboration et al., 2016, *A&A*, 595, A1
- Gaia Collaboration Brown A. G. A., Vallenari A., Prusti T., de Bruijne J. H. J., Babusiaux C., Bailer-Jones C. A. L., 2018, preprint, ([arXiv:1804.09365](https://arxiv.org/abs/1804.09365))
- García R. A., et al., 2011, *MNRAS*, 414, L6
- Gilliland R. L., et al., 2010, *PASP*, 122, 131
- Girardi L., 2016, *ARA&A*, 54, 95
- Gustafsson B., Edvardsson B., Eriksson K., Jørgensen U. G., Nordlund Å., Plez B., 2008, *A&A*, 486, 951
- Harvey J., 1985, in Rolfe E., Battrick B., eds, *ESA Special Publication Vol. 235, Future Missions in Solar, Heliospheric & Space Plasma Physics*.
- Hawkins K., et al., 2016a, *A&A*, 592, A70
- Hawkins K., et al., 2016b, *A&A*, 592, A70
- Hawkins K., Masseron T., Jofré P., Gilmore G., Elsworth Y., Hekker S., 2016c, *A&A*, 594, A43
- Hawkins K., Leistedt B., Bovy J., Hogg D. W., 2017, *MNRAS*, 471, 722
- Heiter U., Jofré P., Gustafsson B., Korn A. J., Soubiran C., Thévenin F., 2015, *A&A*, 582, A49
- Hinkel N. R., Timmes F. X., Young P. A., Pagano M. D., Turnbull M. C., 2014, *AJ*, 148, 54
- Hjørringgaard J. G., Silva Aguirre V., White T. R., Huber D., Pope B. J. S., Casagrande L., Justesen A. B., Christensen-Dalsgaard J., 2017, *MNRAS*, 464, 3713
- Howell S. B., et al., 2014, *PASP*, 126, 398
- Huber D., et al., 2012, *ApJ*, 760, 32
- Huber D., et al., 2013, *ApJ*, 767, 127
- Jofré P., 2016, *Astronomische Nachrichten*, 337, 859
- Jofré P., et al., 2014, *A&A*, 564, A133
- Jofré P., et al., 2015, *A&A*, 582, A81
- Jofré P., et al., 2017, *A&A*, 601, A38
- Jones E., Oliphant T., Peterson P., Others 2001, *SciPy: Open source scientific tools for Python*, <http://www.scipy.org/>
- Kallinger T., et al., 2014, *A&A*, 570, A41
- Kjeldsen H., Bedding T. R., 1995, *A&A*, 293, 87
- Koch D. G., et al., 2010, *ApJ*, 713, L79
- Kolodziejczak J., Caldwell D., 2011, Technical Report 20120003045, Science from Kepler Collateral Data: 150 ksec/year from 13 Million Stars?, <http://ntrs.nasa.gov/archive/nasa/casi.ntrs.nasa.gov/20120003045.pdf>. NASA Marshall Space Flight Centre, <http://ntrs.nasa.gov/archive/nasa/casi.ntrs.nasa.gov/20120003045.pdf>
- Lindgren L., et al., 2018, preprint, ([arXiv:1804.09366](https://arxiv.org/abs/1804.09366))
- Lomb N. R., 1976, *Ap&SS*, 39, 447
- Lund M. N., et al., 2016, preprint, ([arXiv:1612.00436](https://arxiv.org/abs/1612.00436))
- Masseron T., et al., 2014, *A&A*, 571, A47
- Masseron T., Merle T., Hawkins K., 2016, BACCHUS: Brussels Automatic Code for Characterizing High accuracy Spectra, Astrophysics Source Code Library (ascl:1605.004), doi:10.20356/C4TG6R
- Matteucci F., Recchi S., 2001, *ApJ*, 558, 351
- Montet B. T., Simon J. D., 2016, *ApJ*, 830, L39
- Mosser B., et al., 2012a, *A&A*, 540, A143
- Mosser B., et al., 2012b, *A&A*, 548, A10
- Mosser B., et al., 2014, *A&A*, 572, L5
- Pérez F., Granger B. E., 2007, *Computing in Science and Engineering*, 9, 21
- Petigura E. A., Marcy G. W., 2012, *PASP*, 124, 1073
- Pinsonneault M. H., et al., 2014, *ApJS*, 215, 19
- Plez B., 2012, Turbospectrum: Code for spectral synthesis, Astrophysics Source Code Library (ascl:1205.004)
- Pope B. J. S., et al., 2016, *MNRAS*, 455, L36
- Ruiz-Dern L., Babusiaux C., Arenou F., Turon C., Lallement R., 2018, *A&A*, 609, A116
- Saio H., Kurtz D. W., Murphy S. J., Antoci V. L., Lee U., 2018, *MNRAS*, 474, 2774
- Scargle J. D., 1982, *ApJ*, 263, 835
- Schaefer B. E., 2016, *ApJ*, 822, L34
- Silva Aguirre V., et al., 2013, *ApJ*, 769, 141
- Silva Aguirre V., et al., 2015, *MNRAS*, 452, 2127
- Silva Aguirre V., et al., 2016, preprint, ([arXiv:1611.08776](https://arxiv.org/abs/1611.08776))
- Smith J. C., et al., 2012, *PASP*, 124, 1000
- Stumpe M. C., et al., 2012, *PASP*, 124, 985
- Twicken J. D., Chandrasekaran H., Jenkins J. M., Gunter J. P., Girouard F., Klaus T. C., 2010, in *Software and Cyberinfrastructure for Astronomy*, p. 77401U, doi:10.1117/12.856798
- Van Eylen V., Agentoft C., Lundkvist M. S., Kjeldsen H., Owen J. E., Fulton B. J., Petigura E., Snellen I., 2018, *MNRAS*, 479, 4786
- White T. R., et al., 2013, *MNRAS*, 433, 1262
- White T. R., et al., 2015, in *European Physical Journal Web of Conferences*, p. 06068, doi:10.1051/epjconf/201510106068
- White T. R., et al., 2017, *MNRAS*, 471, 2882
- Wright J. T., 2018, *Research Notes of the American Astronomical Society*, 2, 16
- Wyatt M. C., van Lieshout R., Kennedy G. M., Boyajian T. S., 2018, *MNRAS*, 473, 5286
- van Leeuwen F., 2007, *A&A*, 474, 653
- van Saders J. L., Ceillier T., Metcalfe T. S., Silva Aguirre V., Pinsonneault M. H., García R. A., Mathur S., Davies G. R., 2016, *Nature*, 529, 181

This paper has been typeset from a \LaTeX file prepared by the author.